Catalysis Science & Technology

Influence of Spin State and Electron Configuration on the Active Site and Mechanism for Catalytic Hydrogenation on Metal Cation Catalysts Supported on NU-1000: Insights from Experiments and Microkinetic Modeling

Journal:	*Catalysis Science & Technology*
Manuscript ID	CY-ART-02-2020-000394.R1
Article Type:	Paper
Date Submitted by the Author:	08-May-2020
Complete List of Authors:	Shabbir, Hafeera; Clemson University, Chemical and Biomolecular Engineering Pellizzeri, Steven; Eastern Illinois University, Department of Chemistry and Biochemistry Ferrandon, Magali; Argonne National Laboratory, Chemical Sciences and Engineering Division Kim, In Soo; Korea Institute of Science and Technology, Nanophotonics Research Center Vermeulen, Nicolaas; Northwestern University, Department of Chemistry Farha, Omar; Northwestern University, Chemistry Delferro, Massimiliano; Argonne National Laboratory, Chemical Sciences and Engineering Division Martinson, Alex; Argonne National Laboratory, Materials Science Division Getman, Rachel; Clemson University, Chemical and Biomolecular Engineering

Influence of Spin State and Electron Configuration on the Active Site and Mechanism for Catalytic Hydrogenation on Metal Cation Catalysts Supported on NU-1000: Insights from Experiments and Microkinetic Modeling

Hafeera Shabbir [a], Steven Pellizzeri[b], Magali Ferrandon[c], In Soo Kim[d,e], Nicolaas A. Vermeulen[f], Omar K. Farha[f,*], Massimiliano Delferro[c,*], Alex B.F. Martinson[d,*], Rachel B. Getman[a,*]

[a] Chemical and Biomolecular Engineering, Clemson University, Clemson, SC 29634, USA.

[b] Department of Chemistry and Biochemistry, Eastern Illinois University, Charleston, IL 61920, USA.

[c] Chemical Sciences and Engineering Division, Argonne National Laboratory, Argonne, IL 60439, USA.

[d] Materials Science Division, Argonne National Laboratory, Argonne, IL 60439, USA.

[e] Present address: Nanophotonics Research Center, Korea Institute of Science and Technology, Seoul 02792, South Korea.

[f] Department of Chemistry and International Institute for Nanotechnology, Northwestern University, 2145 Sheridan Road, Evanston, IL 60208, USA.

**corresponding authors*

Abstract

The mechanism of ethene hydrogenation to ethane on six dicationic 3*d* transition metal catalysts is investigated. Specifically, a combination of density functional theory (DFT), microkinetic modeling, and high throughput reactor experiments is used to interrogate the active sites and mechanisms for Mn@NU-1000, Fe@NU-1000, Co@NU-1000, Ni@NU-1000, Cu@NU-1000, and Zn@NU-1000 catalysts, where NU-1000 is a metal-organic framework (MOF) capable of supporting metal cation catalysts. The combination of experiments and simulations suggests that the reaction mechanism is influenced by the electron configuration and spin state of the metal cations as well as the amount of hydrogen that is adsorbed. Specifically, Ni@NU-1000, Cu@NU-1000, and Zn@NU-1000, which have more electrons in their *d* shells and operate in lower spin states, utilize a metal hydride active site and follow a mechanism where the metal cation binds with one or more species at all steps, whereas Mn@NU-1000, Fe@NU-1000, and Co@NU-1000, which have fewer electrons in their *d* shells and operate in higher spin states, utilize a bare metal cation active site and follow a mechanism where the number of species that bind to the metal cation is minimized. Instead of binding with the metal cation, catalytic species bind with oxo ligands from the NU-1000 support, as this enables more facile H_2 adsorption. The results reveal opportunities for tuning activity and selectivity for hydrogenation on metal cation catalysts by tuning the properties that influence hydrogen content and spin, including the metal cations themselves, the ligands, the binding environments and supports, and/or the gas phase partial pressures.

1 Introduction

A grand challenge in catalysis research is designing catalysts to convert light hydrocarbons in shale gas to denser compounds or platform molecules that can be further converted into fuels and chemicals[1-4]. Specifically, shale gas upgrading is aimed at producing liquid alkanes and short-chain alkenes (e.g. ethene, propylene, and butene). Ideally, catalysts would exist that could produce such products actively and selectively from shale gas under mild reaction conditions, while remaining stable to deactivation (via metal agglomeration or sintering, for example). Designing such catalysts requires combining active and selective catalytic sites with supports that can maintain catalytic stability. While a variety of catalysts have been used for conversion of light hydrocarbons, metal cation catalysts have been relied upon for decades. For example, homogeneous ligated Ni complexes are well-known to promote ethene oligomerization[5], including being used commercially in the Shell Higher Oligomers Process[6], and heterogeneous NiO, $NiSO_4$, and Ni-exchanged zeolite catalysts are active for ethene oligomerization, even under mild reaction conditions[7]. Further, a variety of homogeneous and heterogeneous metal cation-based catalysts are used industrially for hydrocarbon hydrogenation, dehydrogenation, and transfer hydrogenation reactions[8,9]. A goal of this work is to develop design rules for metal cation-based catalysts, in order to learn how to design catalysts that can actively and selectively convert light alkanes in shale gas to liquid alkanes and short-chain alkenes.

Designing catalysts for any reaction requires understanding the reaction mechanism, as this enables the catalyst to be optimized to promote the desired chemistry. Upgrading light hydrocarbons found in natural gas to liquid alkanes and short-chain alkenes requires understanding C-C and C-H bond chemistry; we investigate C-H bond chemistry in this work. Specifically, we interrogate the mechanism of ethene hydrogenation to ethane, C_2H_4 (g) + H_2 (g) → C_2H_6 (g). Given their wide use in promoting reactions involved in upgrading of light hydrocarbons, our study focuses on isolated single-site metal cation-based catalysts, specifically Mn^{2+}, Fe^{2+}, Co^{2+}, Ni^{2+}, Cu^{2+}, and Zn^{2+}. The metal-organic framework (MOF) NU-1000[10] is employed as a catalyst support. MOFs are porous crystals comprised of metal

cation-based nodes connected by organic linker compounds. The nodes of NU-1000 can be post-synthetically modified to install metal cation catalysts[10,11], and these materials (denoted M@NU-1000 catalysts, where M stands for metal cation) have been shown to be active for the methane to methanol, ethene to ethane, ethene to butene, propyne to propylene, and propane to propene reactions[12-17]. Hypothetically, the metal-organic nature and crystalline structure of NU-1000 can maintain spatial and electronic isolation of the metal cations and thus prevent metal agglomeration and sintering.

Despite the growing body of literature on conversions of light hydrocarbons on M@NU-1000 catalysts, relatively little is known about reaction mechanisms. In fact, the only metal cations for which collaborative experiments and simulations have been performed in order to understand the reaction mechanisms are Ni@NU-1000 (ethene hydrogenation and ethene dimerization) and Co@NU-1000 (ethene dimerization).[16,17] There is only one such study for ethene hydrogenation, published by Li and co-workers for Ni@NU-1000 catalysts. Specifically, Li *et al.* used a combination of *in-situ* X-ray absorption spectroscopy (XAS) characterization and density functional theory (DFT) calculations to learn about the mechanism on Ni@NU-1000.[17] They concluded that the mechanism follows a cycle proposed by Schroeder and Wrighton[18] for photocatalytic olefin hydrogenation on homogeneous metal cation complexes. This mechanism, which from here on out, we refer to as the SW mechanism, is illustrated in Figure 1. Briefly, the active site is a metal hydride. Ethene C_2H_4 (g) adsorbs to the active site (1 in Figure 1 and rxn 3, see below) and then reacts with the metal hydride (2 in Figure 1 and rxn 7, see below), forming an ethyl moiety, C_2H_5. Hydrogen H_2 (g) then adsorbs to the active site (3 in Figure 1 and rxn 2, see below) and reacts with C_2H_5 to form ethane C_2H_6 in a concerted H_2 dissociation/C-H bond formation step (4 in Figure 1 and rxn 9, see below). The C_2H_6 then desorbs (5 in Figure 1 and rxn 4, see below) to regenerate the metal hydride.

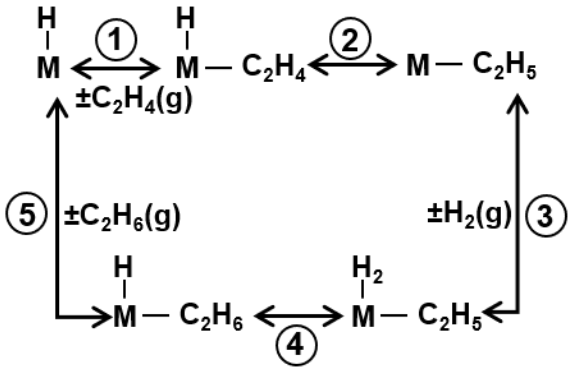

Figure 1. The SW mechanism. M = metal cation.

Our work shows that the metal hydride active site and SW mechanism are not viable for all M@NU-1000 catalysts. Specifically, we use a combination of high throughput reactor experiments, density functional theory calculations, and microkinetic modeling to investigate the mechanism on Mn@NU-1000, Fe@NU-1000, Co@NU-1000, Ni@NU-1000, Cu@NU-1000, and Zn@NU-1000 catalysts. We find that, while valid for Ni@NU-1000, Cu@NU-1000, and Zn@NU-1000 catalysts, the metal hydride active site and SW mechanism are not valid for Mn@NU-1000, Fe@NU-1000, and Co@NU-1000 catalysts. We find that the difference can be attributed to the spin state of the metal cation catalysts. Specifically, metal cations with low spin utilize a metal hydride active site and follow the SW mechanism, whereas metal cations with high spin utilize a bare metal cation active site and follow an alternate mechanism that employs proximal oxo groups for binding of hydrogen species. The switch to the alternate from the SW mechanism is motivated by adsorption of H_2, which becomes endergonic in the SW mechanism on high spin Mn@NU-1000, Fe@NU-1000, and Co@NU-1000. In contrast, H_2 adsorption is exergonic on Mn@NU-1000, Fe@NU-1000, and Co@NU-1000 catalysts in the alternate mechanism.

2 Methods

2.1 Experimental Methods

2.1.1 NU-1000 Synthesis and Post-Modification

NU-1000 synthesis and post-modification with metal cations were carried out using previously reported methods[19,20] which are described in detail in Section S2 in the ESI†. NU-1000 is comprised of $Zr_6(\mu_3\text{-}OH)_4(\mu_3\text{-}O)_4(OH)_4(OH_2)_4$ nodes connected by tetratopic 1,3,6,8-tetrakis(p-benzoate) pyrene linkers (Figure 2a)[21]. Installation of metal cation catalysts occurs at the nodes (circled in Figure 2a) and is accomplished using either vapor phase or solution techniques[10,11]. The vapor phase atomic layer deposition (ALD) in MOFs (AIM) technique is used to create the catalyst samples for this work. Prior to AIM, the Zr_6 nodes present four nearly equivalent faces. Each face has surface chemistry amenable to reaction with up to two metal ALD precursors. According to previously reported processes, AIM results in porous frameworks with 4 to 8 installed metal ions per Zr_6 node[11]; therefore, each face comprises 1 or 2 metal cations. As ALD exhibits self-limiting surface reactions, a route to more than 2 metal cations per face is not obvious and not supported by X-ray total scattering pair distribution function analysis or BET differential pore volume[19]. The installed metal ions replace two protons on a set of hydroxy/water ligands on the node but do not replace the Zr ions. After metal cation installation, the $Zr_6(\mu_3\text{-}OH)_4(\mu_3\text{-}O)_4(OH)_4(OH_2)_4$ coordination environment and the NU-1000 crystallinity is largely retained, with the exception of Fe@NU-1000 and Ni@NU-1000, which show significant amorphization. The large unmodified NU-1000 surface area (2320 m^2/cm^3) is moderately reduced (to 1325 - 2212 m^2/cm^3) as result of processing for these catalysts.

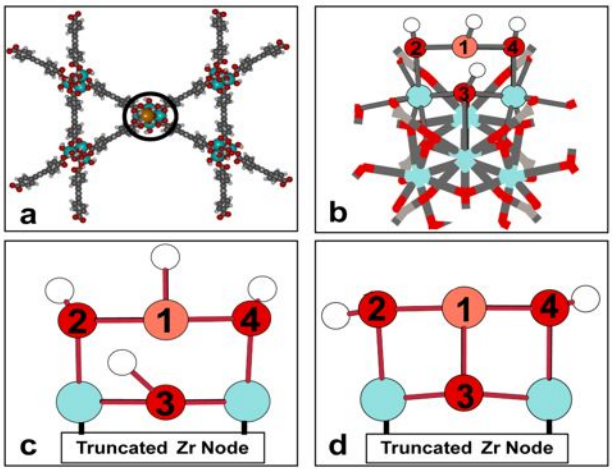

Figure 2. a) The NU-1000 crystal structure with the node circled. b) The catalyst model employed in this work. c) Metal hydride active site. d) Bare metal cation active site. Color key: carbon = gray, oxygen = red, hydrogen = white, zirconium = teal, metal cation = orange. In b), c) and d), atoms labeled 1, 2, 3, and 4 represent the different sites where hydrogen species are allowed to bind in the density functional theory calculations.

2.1.2 Catalytic Experiments

Catalytic experiments in this work utilize a 16-channel high-throughput fixed bed system (Flowrence® from Avantium). 10 mg catalyst are mixed with 50 mg Silica Davisil (230-400 mesh, Sigma-Aldrich) and loaded into a quartz reactor (2 mm ID, 30 mm length). The catalysts are first pre-treated with 3% H_2/Ar at 200 °C for 2 h (10°C/min). For the reaction, total flowrates of 30.0 mL/min are fed, comprising 7.5 mL/min 3% ethene/Ar, 21.5 mL/min 3% H_2/Ar, and 1 mL/min He as an internal standard. Conversions are held to below 10% in most cases, with some exceptions, mainly involving Ni@NU-1000 (see Table S5 in the ESI†). All gases are purchased from Airgas and are UHP grade and have oxygen and moisture traps. Temperatures span from 50 to 200 °C (2 °C/min) with an increment of 25 °C. At each temperature, gas samples are taken automatically and sequentially, starting with reactor #1 and ending with reactor #16, for gas chromatography. Each gas sample is flushed for 11 min before analysis. A ~100 % carbon balance indicates the only product is ethane.

A reasonable question is whether the installed metals remain cationic during the hydrogenation experiments (i.e., that they resist agglomeration into metal nanoparticles). Prior publications by some of us based on X-ray absorption near edge structure (XANES) and extended X-ray absorption fine structure (EXAFS) on Ni@NU-1000 indicate that the cationic Ni^{2+} state and the corresponding Ni-O bonds are largely preserved after exposure to H_2 at 200 ^oC, with the most major change in the Ni oxo structure being due to formation of a small amount of Ni hydride.[17] Further, XAS and EXAFS of Cu@NU-1000 reveals that the installed Cu remains cationic below 200 ^oC in a H_2 environment.[22] As the free energies of reduction of Mn, Fe, Co, and Zn cations to neutral metals are higher (more positive) than for Ni and Cu, we assume that these metals also retain their cationic states under the hydrogenation conditions employed in our experiments and do not agglomerate into metallic nanoparticles.

2.2 Computational Methods

2.2.1 Catalyst Model

Calculations in this work utilize models comprising a truncated NU-1000 node with an installed metal cation (Figure 2b), similar to prior work[16,17,23]. While there is some question as to whether the NU-1000 node comprises one or more metal cations, prior literature based on DFT analysis of the reaction mechanism of ethylene dimerization at the Ni oxo sites on Ni@NU-1000 catalysts indicates that the Ni cation spin state influences the results more than the nuclearity of the Ni oxo clusters, with models including one Ni cation giving nearly identical results as models comprising four Ni cations, as long as the Ni cations are modeled in the same spin state.[24] Our models thus comprise one metal cation per node. The installed metal cations have formal charges of +2 (i.e., the installed metals are dicationic). Prior to metalation, the truncated node model has a net formal charge of 0. The metal cations take the place of two protons on the node; hence, installation of the metal cations does not change the net formal charge of the model. Catalytic species are allowed to bind to the metal cation along with its proximal oxo and hydroxy ligands. The atoms where catalytic species are allowed to bind make up the active sites in our models. In all, we evaluate five different active sites (illustrated in Figure S1 in the ESI†).

What distinguishes one active site from another is the arrangement of hydrogen species on the metal cation and proximal oxo and hydroxy ligands. Our findings suggest that Mn@NU-1000, Fe@NU-1000, Co@NU-1000, Ni@NU-1000, Cu@NU-1000, and Zn@NU-1000 use the active site compositions illustrated in Figures 2c and 2d for ethene hydrogenation. Specifically, Figure 2c is the metal hydride active site utilized in the SW mechanism by Ni@NU-1000,[17] Cu@NU-1000, and Zn@NU-1000, and Figure 2d shows the bare metal cation active site identified in this work as being utilized by Mn@NU-1000, Fe@NU-1000, and Co@NU-1000.

2.2.2 Reaction Steps

In all, we evaluate 22 reaction steps for each M@NU-1000 catalyst using microkinetic modeling. Nine of the reaction steps that we consider are illustrated in Figure 3 and listed below. The rest are described in the ESI† in Figures S2 and S3 and Table S2. Reaction steps that utilize the "/" notation (e.g., rxns 2, 3, 4 and 7 listed below) denote co-adsorption, as in prior work[23]. For example, (H_2/C_2H_5)-M in rxns 2 and 9 indicates that H_2 and C_2H_5 are co-adsorbed to the metal cation site. The steps shown in Figure 3 and listed below are the ones identified in microkinetic modeling as belonging to a reaction mechanism followed by the catalysts studied in this work. Reaction steps within the SW mechanism are highlighted in Figure 3.

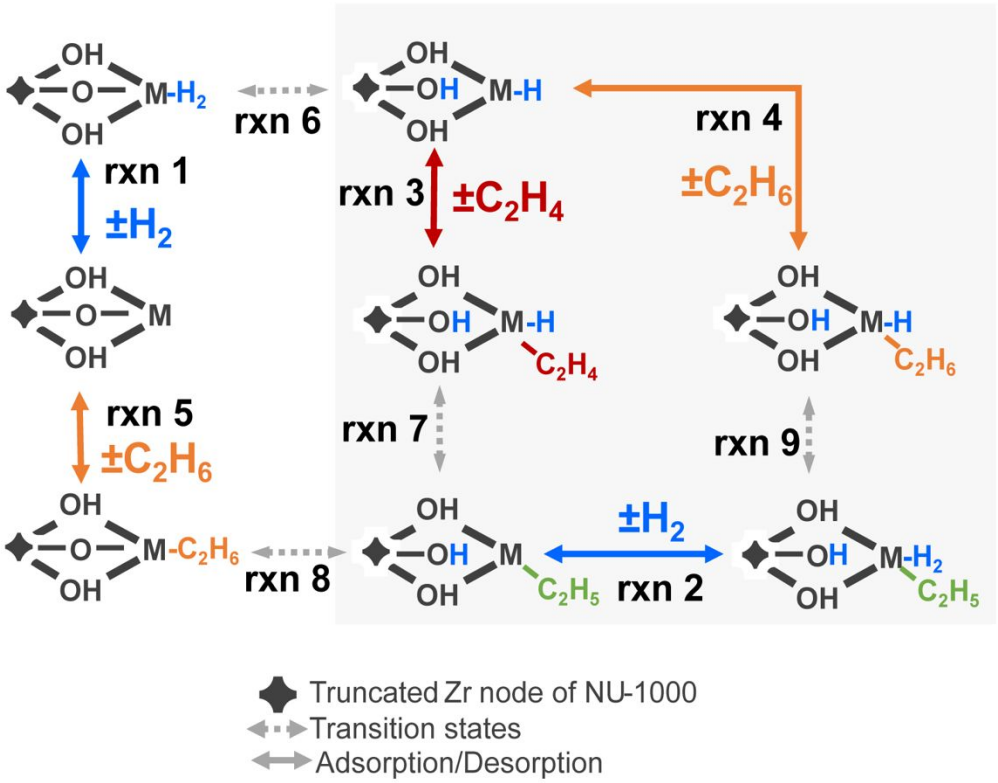

Figure 3. Reaction steps followed by the metal cation catalysts studied in this work. Rxn numbers correspond to those in the text. The SW mechanism is highlighted.

Adsorption/Desorption:

$$M + H_2\,(g) \leftrightarrow H_2\text{-}M \qquad \text{(rxn 1)}$$

$$C_2H_5\text{-}M + H_2\,(g) \leftrightarrow (H_2/C_2H_5)\text{-}M \qquad \text{(rxn 2)}$$

$$H\text{-}M + C_2H_4\,(g) \leftrightarrow (H/C_2H_4)\text{-}M \qquad \text{(rxn 3)}$$

$$H\text{-}M + C_2H_6\,(g) \leftrightarrow (H/C_2H_6)\text{-}M \qquad \text{(rxn 4)}$$

$$M + C_2H_6\,(g) \leftrightarrow C_2H_6\text{-}M \qquad \text{(rxn 5)}$$

H_2 Dissociation:

$$H_2\text{-}M + O_{site\ 3} \leftrightarrow H\text{-}M + H\text{-}O_{site\ 3} \qquad \text{(rxn 6)}$$

C-H Bond Formation:

$$(H/C_2H_4)\text{-}M \leftrightarrow C_2H_5\text{-}M \quad \text{(rxn 7)}$$

$$C_2H_5\text{-}M + H\text{-}O_{site\ 3} \leftrightarrow C_2H_6\text{-}M + O_{site\ 3} \quad \text{(rxn 8)}$$

Concerted H_2 Dissociation/C-H Formation:

$$(H_2/C_2H_5)\text{-}M \leftrightarrow (H/C_2H_6)\text{-}M \quad \text{(rxn 9)}$$

2.2.3 Microkinetic Modeling

Microkinetic modeling is carried out using the MKMCXX program[25-27]. Similar to experiments, microkinetic models are run over temperature ranges of 50-200°C. The total pressure is set to atmospheric and comprises 0.75% ethene and 2.25% hydrogen in a balance of inert gas. All pressures are held constant over the course of simulation. Since ethane is not introduced into the system, this represents the case where the % conversion of ethene equals zero. Each simulation is run for 10^8 s and considered to be converged when the changes in the fractional concentrations of all of the reaction intermediates between successive iterations are less than 10^{-12}. Adsorption (k_{ads}) and desorption (k_{des}) rate constants are calculated as[27]

$$k_{ads} = \frac{yPA}{\sqrt{2\pi m k_b T}} \quad \text{(eq. 1)}$$

$$k_{des} = \frac{k_b T^3}{h^3} * \frac{A(2\pi m k_b)}{\sigma \Theta_{rot}} * e^{-\frac{E_{des}}{k_b T}} \quad \text{(eq. 2)}$$

where y is mole fraction; P is total pressure; A is the surface area of the adsorption site; m is molecular mass; k_b is Boltzmann's constant; T is temperature; σ is symmetry number for rotations and Θ_{rot} is the characteristic rotation temperature[27-29]; h is Planck's constant; and E_{des} is the zero-point (ZP) corrected energy of desorption, which is calculated with DFT. In cases where E_{des} is negative, it is set to zero in

eq. 2. The adsorption site surface area A is estimated with Multiwfn [30,31] using the electrostatic potential of an isolated metal cation calculated in DFT. Multiwfn computes the surface area of the cation using the electrostatic potential on its van der Waals surface. The assumptions underlying construction of k_{des} and k_{ads} are as follows: 1) gas phase molecules are assumed to be ideal, 2) catalytic species possess vibrational but no translational or rotational degrees of freedom, and 3) adsorption and desorption proceed through a "mobile precursor" which possesses two translational degrees of freedom and full rotational and vibrational degrees of freedom. Translational, rotational, and vibrational partition functions for gas molecules are calculated using the particle in a box/particle on a plane, rigid rotor, and harmonic oscillator models, respectively, and vibrational partition functions for catalytic species are calculated with the harmonic oscillator model. Thermal effects due to vibration upon adsorption/desorption are assumed to be negligible with respect to thermal effects due to translation and rotation; hence, eq. 2 assumes the ratio of vibrational partition functions between the mobile precursor and the gas molecule is ~ 1. These assumptions are illustrated in detail Section S4 of the ESI†. Rate constants for surface reactions are calculated as

$$k_{surf} = \frac{k_b T Q^{TS}}{h \quad Q} e^{-\frac{E_a}{k_b T}} \qquad \text{(eq. 3)}$$

where E_a is the activation barrier calculated in DFT, and Q^{TS} and Q are the vibrational partition functions for the transition state and reactant, respectively. In cases where $E_a < 0$, it is set to 0 in eq. 3.

All partition functions used in microkinetic modeling are calculated with the TAMkin software[32]. Vibrational partition functions are constructed using frequencies calculated in DFT. Specifically, the partition functions are constructed using frequencies associated with the atoms in the adsorbed species and the active site only. All frequencies with values below 50 cm^{-1} are replaced with 50 cm^{-1} to correct for the overestimation of the entropy contribution due to the known breakdown of the harmonic oscillator approximation for low-frequency vibrational modes[33]. Further, all frequencies with

values above 50 cm^{-1} are scaled by 0.976, as in prior work[23], due to the tendency of the DFT method to overestimate vibrational frequencies[34,35].

2.2.4 DFT Calculations

Structures, energies, and vibrational frequencies are calculated using the Gaussian09 software[36]. Electron exchange and correlation are modeled using the M06-L density functional[37,38]. Wavefunctions are expanded using the Def2-SVP basis set for H, C, and O atoms; the Def2-TZVPP basis set for the metal cation catalyst (M); and the Def2-TZVPP basis set with the associated effective core potential for the Zr cations.[16,23,39,40] The total charge on the truncated node models with installed cations is set to 0 in all DFT calculations. During geometry optimizations and transition state searches involving NU-1000, the carbon atoms on the benzoate groups on the catalyst model are kept fixed to simulate the structural rigidity of the NU-1000 framework[23,40]. The Berny algorithm[41] is used for both geometry optimizations and transition state searches along with the default convergence criteria. Vibrational frequencies are calculated for all structures both to verify their natures as local minima or transition states on the potential energy surface and to determine the vibrational partition functions used for the microkinetic model.

Multiple possible spin-states for Mn@NU-1000, Fe@NU-1000, Co@NU-1000, and Ni@NU-1000 are considered (Cu^{2+} and Zn^{2+} only have one possible spin state each, i.e., doublet and singlet, respectively; hence Cu@NU-1000 and Zn@NU-1000 are only modeled in these spin states.) Specifically, Mn@NU-1000 is modeled as a quartet and a sextet, Fe@NU-1000 as a triplet and a quintet, Co@NU-1000 as a doublet and a quartet, and Ni@NU-1000 as a singlet and a triplet. We did not include the doublet and singlet structures for Mn@NU-1000 and Fe@NU-1000, since these spin states are not energetically favorable. Unless indicated otherwise, microkinetic modeling results use the spin state that gives the lowest energy for each structure, as in prior work[23]. For these intermediates, the total spin is within 10% of the expected values, indicating minimal spin contamination. The calculated energies

of all catalytic species considered in this work are provided in Tables S3 and S4 in the ESI†; further, Gaussian log files are available on GitHub[42].

3. Results

The rates of ethane formation observed in high throughput reactor studies and calculated in microkinetic modeling are plotted as functions of temperature in Figure 4. The experimental rates (Figure 4a) include contributions from the metal cations as well as from NU-1000 itself; catalytic studies performed on a non-metallated NU-1000 sample indicate NU-1000 contributes ~ 10^{-10} moles of ethane produced per second to the observed rates, compared to ~ 10^{-7} moles of ethane produced per second on Ni@NU-1000 and ~ 10^{-9} moles of ethane produced per second on Cu@NU-1000. Simulated rates using the SW mechanism (5 total rxn steps; see Figures 1 and 3) are plotted in Figure 4b. Comparing Figures 4a and 4b, Ni@NU-1000 gives the highest rate of all the metals, while Zn@NU-1000 gives the lowest. The rank order for rate observed experimentally is Ni@NU-1000 > Co@NU-1000 > Cu@NU-1000 > Mn@NU-1000 > Fe@NU-1000 > Zn@NU-1000, whereas the trend simulated using the SW mechanism is Ni@NU-1000 > Cu@NU-1000 ~ Mn@NU-1000 ~ Fe@NU-1000 > Co@NU-1000 > Zn@NU-1000. Notably, Co@NU-1000 is observed experimentally to exhibit a high rate; however, in Figure 4b, Co@NU-1000 exhibits a relatively low rate. This disagreement between experiment and simulations prompted us to explore the expanded reaction network involving proximal oxo/hydroxy groups discussed above (22 total rxn steps; see Figure S2 in the ESI†). In doing this, the mechanism for each catalyst is revealed in microkinetic modeling, which reduces the number of assumptions in the simulations. Simulated rates employing the expanded reaction network are shown in Figure 4c. Using this expanded reaction network, the rank order for rate is Ni@NU-1000 > Mn@NU-1000 > Co@NU-1000 > Fe@NU-1000 > Cu@NU-1000 > Zn@NU-1000. Notably, using the expanded reaction network, Co@NU-1000 exhibits a high rate, as observed experimentally. The experimental trend in catalytic activity is also more closely reproduced, with the exception of Mn@NU-1000.

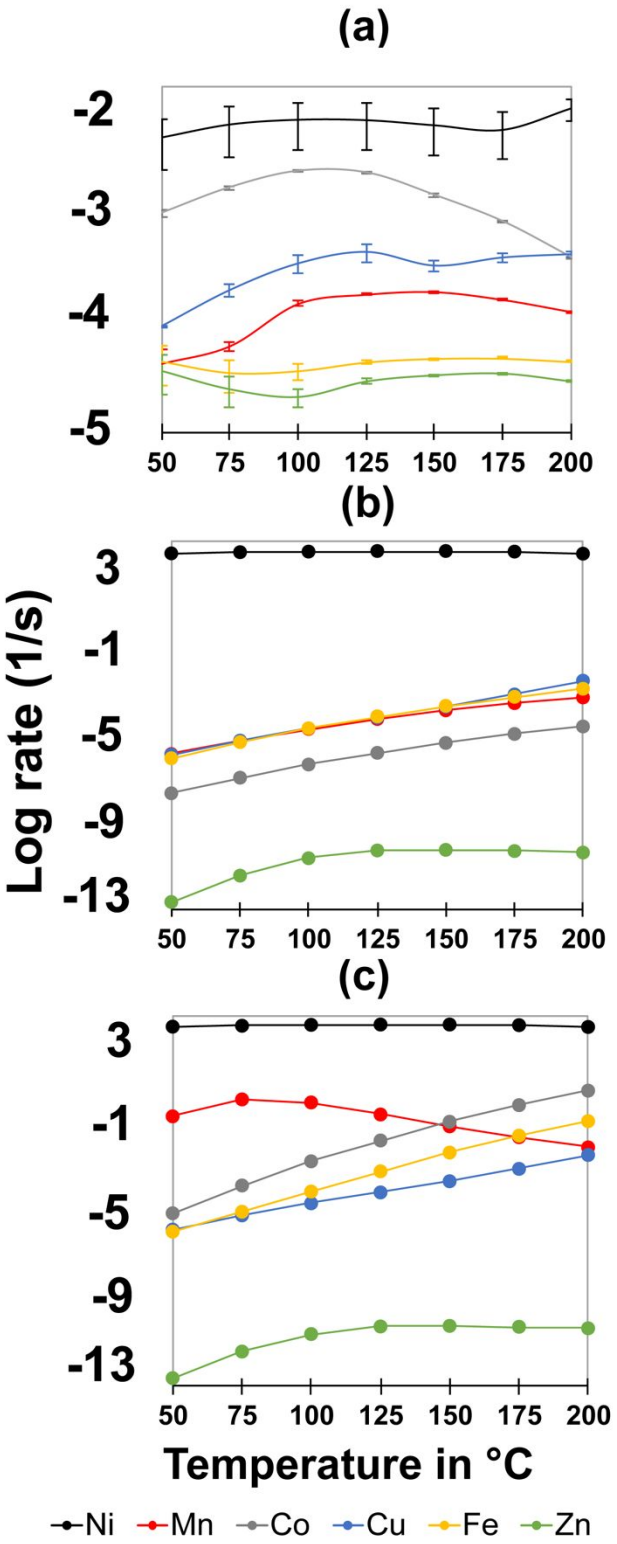

Figure 4. Log rates in units of moles of ethene converted per metal cation site per second. (a) Experimentally measured. (b) Rates simulated in microkinetic modeling including only the 5 steps that comprise the SW mechanism. (c) Rates simulated using all 22 steps considered in this work.

Analysis of the microkinetic modeling results indicates that Ni@NU-1000, Cu@NU-1000, and Zn@NU-1000 follow the SW mechanism (Cu@NU-1000 actually follows the SW mechanism up to 150°C, above which it follows a different mechanism; see Section S1 in the ESI†), while Mn@NU-1000, Fe@NU-1000, and Co@NU-1000 follow an alternate mechanism, illustrated in Figure 3. This mechanism starts from a bare metal cation active site (Figure 2d). H_2 adsorbs to this site (rxn 1) and dissociates via the use of a proximal oxo ligand (rxn 6), forming a metal hydride and converting the oxo to a hydroxy ligand. C_2H_4 adsorbs to (rxn 3) and reacts with the hydride (rxn 7), forming C_2H_5. The C_2H_5 then reacts with the residual H from the proximal hydroxyl ligand to form C_2H_6 (rxn 8), which then desorbs (rxn 5) to regenerate the bare metal cation catalyst.

4. Discussion

4.4.1 Rationale for Mechanism Preference

In their lowest energy configurations, the preference of the different metal cations for the SW mechanism versus the alternate mechanism depends on the occupancy of the *d* shell of the metal cation. Specifically, Ni@NU-1000, Cu@NU-1000, and Zn@NU-1000, which have more electrons in their *d* shells, prefer the SW mechanism, whereas Mn@NU-1000, Fe@NU-1000, and Co@NU-1000, which have fewer electrons in their *d* shells, prefer the alternate mechanism. We show below that the preference for the SW or alternate mechanism depends on both the occupancy of the *d* shell and the spin state of the metal cation.

Of the M@NU-1000 catalysts that we studied, the lowest energy structures are for the most part high spin states (see Table S3 in the ESI†), meaning that the energy separation between neighboring *d* orbitals is small enough such that it facilitates putting electrons into higher energy orbitals rather than putting two into the same low-energy orbital, thereby allowing for a greater distribution of electron density across all of the *d* orbitals as compared to a low spin state. (The exceptions are Ni@NU-1000, which prefers the singlet state for all structures except the metal hydride, the transition state for rxn 7

on Co@NU-1000, which prefers the doublet spin state, and Cu@NU-1000 and Zn@NU-1000, which can only exist in one spin state, due to being d^9 and d^{10} complexes, respectively.) To interrogate how this influences the mechanism, we re-ran our microkinetic model, this time instead of using the spin states that gave the lowest energy for each structure, we exclusively ran each spin state for each M@NU-1000 catalyst. The results (Table 1 and Figure S5 in the ESI†) suggest that metals in low spin states prefer the SW mechanism, whereas metals in high spin states prefer the alternate mechanism. The switch of preference from the SW mechanism to the alternate mechanism happens at the quartet spin state. Catalysts that can assume this spin state are Mn@NU-1000 and Co@NU-1000. While the Co@NU-1000 quartet prefers the alternate mechanism, the Mn@NU-1000 quartet prefers the SW mechanism, suggesting that the mechanism depends both on the spin state and the electron configuration of the metal cation. In this case, Mn@NU-1000, which has fewer *d* electrons, prefers the SW mechanism, while Co@NU-1000, which has more *d* electrons, prefers the alternate mechanism.

Table 1. Mechanism and active site preference for the different spin states considered in this work.

Catalyst	Spin State	Preferred Mechanism and Active Site
Mn@NU-1000	Quartet	SW
"	Sextet	Alternate
Fe@NU-1000	Triplet	SW
"	Quintet	Alternate
Co@NU-1000	Doublet	SW
"	Quartet	Alternate
Ni@NU-1000	Singlet	SW
"	Triplet	SW
Cu@NU-1000	Doublet	SW[a]
Zn@NU-1000	Singlet	SW

[a] $T \leq 150$ °C. Above 150 °C, Cu@NU-1000 follows an alternate mechanism. Further details are provided in ESI† Figure S6.

Calculated free energies along the SW and alternate mechanisms for Mn@NU-1000, Fe@NU-1000, and Co@NU-1000 are compared in Figure 5. Analysis of these values suggests that the alternate mechanism exhibits faster rates because it provides a lower energy route for H_2 adsorption. Free energies for H_2 adsorption in the SW mechanism (rxn 2) are compared with those in the alternate

mechanism (rxn 1) in Table 2. Specifically, H_2 adsorption in the SW mechanism is endergonic on Mn@NU-1000, Fe@NU-1000, and Co@NU-1000, while H_2 adsorption in the alternate mechanism is exergonic on Mn@NU-1000, Fe@NU-1000, and Co@NU-1000. The low driving force for H_2 adsorption in the SW mechanism results in a lower hydrogenation rate. Prior literature on low spin Ni@NU-1000 versus high spin Co@NU-1000 catalysts for C_2H_4 dimerization indicates that the low spin Ni@NU-1000 catalyst is more active, since the greater availability (lower filling) of *d* orbitals allows more effective binding with catalytic species[16]. Specifically, using state-of-the-art multireference calculations, Bernales and co-workers showed that the low spin Ni@NU-1000 catalyst more effectively binds with C_2H_4 due to the availability of an unoccupied *d* orbital, which leads to a lower transition barrier for C-C bond formation. A similar argument could be made here for the case of H_2 adsorption in the alternate mechanism versus the SW mechanism. In the SW mechanism, H_2 adsorption (rxn 2) takes place on a metal cation with an adsorbed ethyl moiety. As the ethyl moiety is chemically bonded to the metal cation, it hybridizes with metal cation *d* electron density. This makes the metal cation less effective at binding with H_2. Indeed, Mulliken population analysis (see Table S4 in the ESI†) indicates that the bare metal cations in the Mn@NU-1000, Fe@NU-1000, and Co@NU-1000 catalysts have fewer *d* electrons, and hence a greater fraction of unoccupied *d* orbitals, than their analogs with adsorbed C_2H_5. Additionally, metal cation-H_2 bond distances are shorter on the bare metal cations than on the metal cations with adsorbed C_2H_5 (see Table S4 in the ESI†), further corroborating more effective hybridization on the bare metal cation sites. These results suggest that high spin metals prefer the alternate mechanism for hydrogenation because the bare metal cation site is more effective at binding H_2, which results in more favorable H_2 adsorption free energies and hence faster rates.

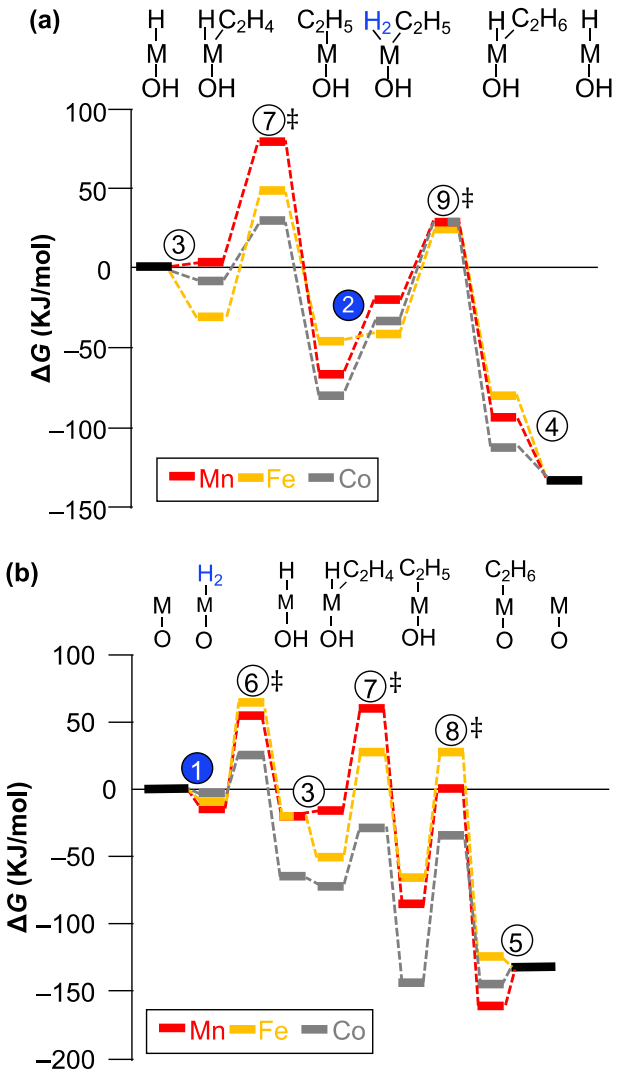

Figure 5. Calculated free energies along the SW (a) and alternate (b) mechanisms. Rxn numbers correspond to the text and are circled; circles for rxns involving H_2 adsorption are shaded blue. ‡ denote transition states.

Table 2. Calculated H_2 adsorption free energies on the metal hydride (rxn 2) versus bare metal cation (rxn 1) for Mn, Fe, and Co@NU-1000 catalysts in kJ/mol. Endergonic values are bolded.

	Mn@NU-1000	Fe@NU-1000	Co@NU-1000
SW (rxn 2)	**ΔG = 46**	**ΔG = 4**	**ΔG = 47**
Alternate (rxn 1)	ΔG = –13	ΔG = –9	ΔG = –3

4.4.2 Comparison of Apparent Activation Energies

To further test the validities of the proposed mechanisms, we compared measured apparent activation energies with simulated values from microkinetic modeling. Apparent activation energies were calculated for Mn@NU-1000, Co@NU-1000, Ni@NU-1000, and Cu@NU-1000 catalysts (Table 3) between 50 ^{o}C and either 75 ^{o}C or 100 ^{o}C (see the ESI†), i.e., the regions in Figures 4a and 4c where the rate either increases or remains ~ constant with temperature. Details on how these values were calculated are provided in Section S5 of the ESI†. Insights from microkinetic modeling indicate that the catalysts are adsorption limited over the temperature range studied; this causes the rate to come to a maximum and then start decreasing with temperature. Such trends are seen in both the experimentally observed (Figure 4a) and simulated (Figure 4c) rates. Hence, the apparent activation energies could have contributions from the activation barrier of the rate controlling step as well as from the energy of desorption. From Table 3, the trend in the experimentally measured apparent activation energies is Cu@NU-1000 ~ Mn@NU-1000 < Co@NU-1000 < Ni@NU-1000. The value for Ni@NU-1000 is in good agreement from previously reported studies[17]. The trend in the apparent activation energies derived from microkinetic modeling is Ni@NU-1000 < Cu@NU-1000 ~ Mn@NU-1000 < Co@NU-1000. Ni@NU-1000 is hence predicted by microkinetic modeling to have a relatively low apparent activation energy, while it is observed experimentally to have a high apparent activation energy; otherwise, the experimental and simulated trends are the same. Notably, Ni@NU-1000 is controlled largely by adsorption/desorption in the microkinetic modeling results. Comparing the apparent activation energy values between experiments and theory indicates a factor of at least 3.5 and to up to 6.6 between experiments and theory. The largest discrepancy is for Ni@NU-1000; we note that the highest activation barrier in the dominant reaction pathway for Ni@NU-1000 is 17 kJ/mol, which is in much better agreement with experiment. The discrepancy for the rest of the metals could be for multiple reasons. For example, even small differences in the energy of desorption between simulations and experiments could create significant inconsistencies in the temperature at which the catalysts become adsorption limited and thus how much of the apparent activation energy is due to desorption versus

surface reaction (as in the case of Ni@NU-1000). Further, there could be steps with lower barriers than those proposed in this manuscript (e.g., a lower barrier alternative to rxn 8 on Co@NU-1000), which have not yet been identified. In fact, some of the complexity in fully reconciling the mechanisms of M@NU-1000 catalysts is due to spin: calculating energetics of catalytic species when there are multiple spin states possibly at play is computationally demanding (requiring multireference calculations) and theoretically challenging. In this work, we identify the influence that spin has on H_2 adsorption; fully understanding the mechanisms of C-C and C-H bond chemistry on M@NU-1000 catalysts remains a significant focus of our ongoing work.

Table 3. Apparent activation energies Mn, Co, Ni, and Cu@NU-1000 catalysts in kJ/mol.

	Mn@NU-1000	Co@NU-1000	Ni@NU-1000	Cu@NU-1000
Experiment	16	20	25	15
Microkinetic modeling	58	110	4	56

5. Conclusions

In this work, we performed high throughput reactor studies and microkinetic modeling to investigate the mechanism of ethene hydrogenation on metal cation catalysts supported on the MOF NU-1000. We found that metal cations with smaller numbers of unpaired electrons utilize a metal hydride active site and follow a mechanism previously proposed for catalytic hydrogenation on M@NU-1000 catalysts and homogeneous metal cation photocatalysts. In contrast, metal cations that have more unpaired electrons utilize a bare metal cation active site and employ proximal oxo ligands for binding of hydrogen species. Similar to prior work[16], the high spin metal cations seek mechanisms where the availability of unoccupied *d* orbitals is maximized, as this improves the hybridization with orbitals of gas phase species. In the case of catalytic hydrogenation, this leads to more effective binding of H_2.

While these conclusions provide valuable insights about the mechanism of C-H bond chemistry on M@NU-1000 catalysts, state-of-the-art multireference calculations are needed to accurately calculate the energetics of spin polarized metal cations[43-45]. Still, these results point to spin as a design

variable for tuning the energies of catalytic intermediates. One can envision tuning activity and selectivity through spin, e.g., by varying the ligands, binding environments, supports, or metal cations, themselves. Further, these results point to partial pressure (e.g., of H_2) as possible "knob" for tuning catalytic activity. Specifically, this work indicates that the rate of catalytic hydrogenation on metal cation catalysts is influenced by the presence (Figure 2c) or absence (Figure 2d) of H* in the base catalyst. One can imagine tuning the H_2 pressure in order to convert a bare metal cation to a metal hydride or vice versa, hence altering the mechanism and rate of catalytic hydrogenation. There are clear opportunities for optimizing catalytic activity and selectivity on metal cation catalysts. These topics are the subjects of ongoing work by our team.

Acknowledgments. This work was supported as part of the Inorganometallic Catalyst Design Center, an Energy Frontier Research Center funded by the US Department of Energy, Office of Science, Basic Energy Sciences, under award DE-SC0012702. The authors thank Lisa Zeeb for making some of the figures presented in this manuscript. RBG thanks Jesse Bond (Syracuse University) for helpful conversations. The authors thank one of the anonymous referees of this manuscript for the suggestion to compare apparent activation energies between experiments and theory.

Conflicts of interest. Omar K. Farha is a shareholder in NuMat Technologies.

†Electronic Supporting Information available: Further details about active sites and mechanisms considered in microkinetic modeling, synthesis and post-modification of NU-1000 including statements about safety and hazards, tabulated DFT and experimental data not included in the manuscript, derivation of rate constants used in microkinetic modeling, details about apparent activation energy calculations.

References

1 D. A. Wood, C. Nwaoha and B. F. Towler, *Gas-to-liquids (GTL): A review of an industry offering several routes for monetizing natural gas*, 2012.

2 H. Schulz, *Short history and present trends of Fischer–Tropsch synthesis*, 1999.

3 H. D. Gesser and N. R. Hunter, *Catal. Today,* 1998, **42**, 183-189.

4 B. Guo and A. Ghalambor, *Natural Gas Engineering Handbook*, Gulf Publishing Company, Houston, 2012.

5 F. Speiser, P. Braunstein and L. Saussine, *Acc. Chem. Res.,* 2005, **38**, 784-793.

6 B. Reuben and H. Wittcoff, *J. Chem. Educ.,* 1988, **65**, 605.

7 A. Finiels, F. Fajula and V. Hulea, *Catal. Sci. Technol.,* 2014, **4**, 2412-2426.

8 Sattler, Jesper J. H. B, J. Ruiz-Martinez, E. Santillan-Jimenez and B. M. Weckhuysen, *Chem. Rev.,* 2014, **114**, 10613-10653.

9 B. Maji and M. K. Barman, *Synth.,* 2017, **49**, 3377-3393.

10 T. C. Wang, N. A. Vermeulen, I. S. Kim, A. B. F. Martinson, J. F. Stoddart, J. T. Hupp and O. K. Farha, *Nat. Protoc.,* 2015, **11**, 149.

11 T. Islamoglu, S. Goswami, Z. Li, A. J. Howarth, O. K. Farha and J. T. Hupp, *Acc. Chem. Res.,* 2017, **50**, 805-813.

12 T. Ikuno, J. Zheng, A. Vjunov, M. Sanchez-Sanchez, M. A. Ortuño, D. R. Pahls, J. L. Fulton, D. M. Camaioni, Z. Li, D. Ray, B. L. Mehdi, N. D. Browning, O. K. Farha, J. T. Hupp, C. J. Cramer, L. Gagliardi and J. A. Lercher, *J. Am. Chem. Soc.,* 2017, **139**.

13 S. P. Desai, J. Ye, J. Zheng, M. S. Ferrandon, T. E. Webber, A. E. Platero-Prats, J. Duan, P. Garcia-Holley, D. M. Camaioni, K. W. Chapman, M. Delferro, O. K. Farha, J. L. Fulton, L. Gagliardi, J. A. Lercher, R. L. Penn, A. Stein and C. C. Lu, *J. Am. Chem. Soc.,* 2018, **140**, 15309-15318.

14 S. T. Madrahimov, J. R. Gallagher, G. Zhang, Z. Meinhart, S. J. Garibay, M. Delferro, J. T. Miller, O. K. Farha, J. T. Hupp and S. T. Nguyen, *ACS Catal.,* 2015, **5**, 6713-6718.

15 Z. Li, A. W. Peters, V. Bernales, M. A. Ortuño, N. M. Schweitzer, M. R. DeStefano, L. C. Gallington, A. E. Platero-Prats, K. W. Chapman, C. J. Cramer, L. Gagliardi, J. T. Hupp and O. K. Farha, *ACS Cent. Sci.,* 2017, **3**, 31-38.

16 V. Bernales, A. B. League, Z. Li, N. M. Schweitzer, A. W. Peters, R. K. Carlson, J. T. Hupp, C. J. Cramer, O. K. Farha and L. Gagliardi, *J. Phys. Chem. C,* 2016, **120**, 23576-23583.

17 Z. Li, N. M. Schweitzer, A. B. League, V. Bernales, A. W. Peters, A. Getsoian, T. C. Wang, J. T. Miller, A. Vjunov, J. L. Fulton, J. A. Lercher, C. J. Cramer, L. Gagliardi, J. T. Hupp and O. K. Farha, *J. Am. Chem. Soc.,* 2016, **138**.

18 M. A. Schroeder and M. S. Wrighton, *J. Am. Chem. Soc.,* 1976, **98**, 551-558.

19 I. S. Kim, S. Ahn, N. A. Vermeulen, T. E. Webber, L. C. Gallington, K. W. Chapman, R. L. Penn, J. T. Hupp, O. K. Farha, J. M. Notestein and A. B. F. Martinson, *J. Am. Chem. Soc.,* 2020, **142**, 242-250.

20 T. C. Wang, N. A. Vermeulen, I. S. Kim, A. B. F. Martinson, J. F. Stoddart, J. T. Hupp and O. K. Farha, *Nat. Protoc,* 2016, **11**, 149-162.

21 O. K. Farha, A. Ö Yazaydın, I. Eryazici, C. D. Malliakas, B. G. Hauser, M. G. Kanatzidis, S. T. Nguyen, R. Q. Snurr and J. T. Hupp, *Nat. Chem.,* 2010, **2**, 944-948.

22 A. Halder, S. Lee, B. Yang, M. J. Pellin, S. Vajda, Z. Li, Y. Yang, O. K. Farha and J. T. Hupp, *J. Chem. Phys.,* 2020, **152**, 084703.

23 S. Pellizzeri, M. Barona, V. Bernales, P. Miró, P. Liao, L. Gagliardi, R. Q. Snurr and R. B. Getman, *Catal. Today,* 2018, **312**, 149-157.

24 J. Ye, L. Gagliardi, C. J. Cramer and D. G. Truhlar, *J. Catal.,* 2017, **354**, 278-286.

25 I. A. W. Filot, R. J. P. Broos, van Rijin, J. P. M, van Heugten, G. J. H. A, R. A. van Santen, E. J. M. Hensen and van Rijin, J. P. M, *ACS Catal.,* 2015, **5**, 5453-5467.

26 I. A. W. Filot, R. A. van Santen and E. J. M. Hensen, *Angew. Chem. Int. Ed.,* 2014, **53**, 12746-12750.

27 I. A. W. Filot, *Introduction to microkinetic modeling*, Technische Universiteit Eindhoven, 2018.

28 S. Glasstone, K. J. Laidler and H. Eyring, *The theory of rate processes*, McGraw-Hill, New York, 1941.

29 L. K. Nash, *Elements of Statistical Thermodynamics: Second Edition*, Dover Publications, New York, 2006.

30 T. Lu and F. Chen, *J. Mol. Graph. Model,* 2012, **38**, 314-323.

31 T. Lu and F. Chen, *J. Comput. Chem.,* 2012, **33**, 580-592.

32 A. Ghysels, T. Verstraelen, K. Hemelsoet, M. Waroquier and V. Van Speybroeck, *J. Chem. Inf. Model.,* 2010, **50**, 1736-1750.

33 R. F. Ribeiro, A. V. Marenich, C. J. Cramer and D. G. Truhlar, *J. Phys. Chem. B,* 2011, **115**, 14556-14562.

34 B. A. De Moor, A. Ghysels, M. Reyniers, V. Van Speybroeck, M. Waroquier and G. B. Marin, *J. Chem. Theory Comput.,* 2011, **7**, 1090-1101.

35 I. M. Alecu, J. Zheng, Y. Zhao and D. G. Truhlar, *J. Chem. Theory Comput.,* 2010, **6**, 2872-2887.

36 M. J. Frisch, G. W. Trucks, H. B. Schlegel, G. E. Scuseria, M. A. Robb, J. R. Cheeseman, G. Scalmani, V. Barone, G. A. Petersson, H. Nakatsuji, X. Li, M. Caricato, A. Marenich, J. Bloino, B. G. Janesko, R. Gomperts, B. Mennucci, H. P. Hratchian, J. V. Ortiz, A. F. Izmaylov, J. L. Sonnenberg, D. Williams-Young, F. Ding, F. Lipparini, F. Egidi, J. Goings, B. Peng, A. Petrone, T. Henderson, D. Ranasinghe, V. G. Zakrzewski, J. Gao, N. Rega, G. Zheng, W. Liang, M. Hada, M. Ehara, K. Toyota, R. Fukuda, J. Hasegawa, M. Ishida, T. Nakajima, Y. Honda, O. Kitao, H. Nakai, T. Vreven, K. Throssell, J. A. Montgomery, Jr., J. E. Peralta, F. Ogliaro, M. Bearpark, J. J. Heyd, E. Brothers, K. N. Kudin, V. N. Staroverov, T. Keith, R. Kobayashi, J. Normand, K. Raghavachari, A. Rendell, J. C. Burant, S. S. Iyengar, J. Tomasi, M. Cossi, J. M. Millam, M. Klene, C. Adamo, R. Cammi, J. W. Ochterski, R. L. Martin, K. Morokuma, O. Farkas, J. B. Foresman, and D. J. Fox, *Gaussian 09, Revision A.02*, Gaussian, Inc., Wallingford CT, 2016.

37 D. Truhlar and Y. Zhao, *J. Chem. Phys.,* 2006, **125**, 194101-18.

38 Y. Zhao and D. G. Truhlar, *Acc. Chem. Res.,* 2008, **41**, 157-167.

39 F. Weigend, *Phys. Chem. Chem. Phys.,* 2006, **8**, 1057.

40 F. Weigend and R. Ahlrichs, *Phys. Chem. Chem. Phys.,* 2005, **7**, 3297.

41 X. Li and M. J. Frisch, *J. Chem. Theory Comput.,* 2006, **2**, 835-839.

42 https://github.com/getman-research-group/Ethylene-hydro-log-files.

43 J. N. Harvey, *Phys. Chem. Chem. Phys.,* 2007, **9**, 331-343.

44 C. A. Gaggioli, L. Belpassi, F. Tarantelli, J. N. Harvey and P. Belanzoni, *Chem. Eur. J.,* 2018, **24**, 5006-5015.

45 B. Yang, L. Gagliardi and D. G. Truhlar, *Phys. Chem. Chem. Phys.,* 2018, **20**, 4129-4136.

Spin state is found to determine the mechanism and active site of catalytic hydrogenation on metal cation catalysts